



Manganese oxide phases and morphologies: A study on calcination temperature and atmospheric dependence

Matthias Augustin^{*1,2}, Daniela Fenske¹, Ingo Bardenhagen¹, Anne Westphal¹, Martin Knipper², Thorsten Plaggenborg², Joanna Kolny-Olesiak² and Jürgen Parisi²

Full Research Paper

[Open Access](#)**Address:**

¹Fraunhofer Institute for Manufacturing Technology and Advanced Materials, Wiener Str. 12, 28359 Bremen, Germany and ²Department of Physics, Energy and Semiconductor Research Laboratory, Carl von Ossietzky University of Oldenburg, 26129 Oldenburg, Germany

Email:

Matthias Augustin^{*} - matthias.augustin@ifam.fraunhofer.de

* Corresponding author

Keywords:

electrocatalytic activity; in situ X-ray diffraction; manganese glycolate; manganese oxide nanoparticles; mesoporous α -Mn₂O₃

Beilstein J. Nanotechnol. **2015**, *6*, 47–59.

doi:10.3762/bjnano.6.6

Received: 16 June 2014

Accepted: 03 December 2014

Published: 06 January 2015

This article is part of the Thematic Series "Nanostructures for sensors, electronics, energy and environment II".

Guest Editor: N. Motta

© 2015 Augustin et al; licensee Beilstein-Institut.
License and terms: see end of document.

Abstract

Manganese oxides are one of the most important groups of materials in energy storage science. In order to fully leverage their application potential, precise control of their properties such as particle size, surface area and Mn^{x+} oxidation state is required. Here, Mn₃O₄ and Mn₅O₈ nanoparticles as well as mesoporous α -Mn₂O₃ particles were synthesized by calcination of Mn(II) glycolate nanoparticles obtained through an economical route based on a polyol synthesis. The preparation of the different manganese oxides via one route facilitates assigning actual structure–property relationships. The oxidation process related to the different MnO_x species was observed by in situ X-ray diffraction (XRD) measurements showing time- and temperature-dependent phase transformations occurring during oxidation of the Mn(II) glycolate precursor to α -Mn₂O₃ via Mn₃O₄ and Mn₅O₈ in O₂ atmosphere. Detailed structural and morphological investigations using transmission electron microscopy (TEM) and powder XRD revealed the dependence of the lattice constants and particle sizes of the MnO_x species on the calcination temperature and the presence of an oxidizing or neutral atmosphere. Furthermore, to demonstrate the application potential of the synthesized MnO_x species, we studied their catalytic activity for the oxygen reduction reaction in aprotic media. Linear sweep voltammetry revealed the best performance for the mesoporous α -Mn₂O₃ species.

Introduction

Manganese oxides are a class of inexpensive compounds with a high potential for nanostructuring, which makes them attractive candidates for various applications, for example, as basis ma-

terials in supercapacitors and electrodes for Li-ion accumulators [1-3]. They exhibit high catalytic activity for different oxidation and reduction reactions due to the diversity in their Mn^{x+}

cation oxidation states as well as morphological characteristics [4,5]. Many manganese oxide phases consist of tunnel structures built from MnO_6 octahedra; these tunnels facilitate the access of reactants to the active reaction sites as well as the absorption of small molecules within the structure. The latter property is especially useful for application as molecular sieves and absorbents for the removal of toxic species from waste gases such as carbon monoxide and nitrogen oxide [6-8]. Additionally, manganese oxide structures exhibiting oxygen vacancies provide additional active sites for reduction and oxidation reaction intermediates, especially those involving oxygen. These properties are especially important for catalytic applications such as water oxidation [9-11] and the oxygen reduction and evolution reactions in metal/air battery systems [12-16]. Additionally, the advantages of manganese oxides can be enhanced by nanostructuring of the different species, which was recently shown by Zhang et al. [17]. In their report, better cyclability of Li-ion cells was obtained with anodes consisting of mesoporous Mn_2O_3 particles compared to Mn_2O_3 bulk powder electrodes [17].

Several nanoscale manganese oxide compounds can be prepared via calcination processes from suitable precursors [7,18-20]. Whereas many synthetic protocols yield manganese oxide species at the nanometer scale [21], for example, precipitation or the solvothermal route, these methods require long reaction times in the range of hours (up to 24 h) and subsequent drying processes of up to 2 days [22-27]. The synthesis via oxidation of manganese metal nanoparticles by gas condensation must be followed by annealing in O_2 -containing atmospheres to obtain different manganese oxide species [28]. An advantage of the calcination route, on the other hand, is the conservation of the morphology and size of the precursor during this process, which is of special interest when considering the use of nanoscale precursor particles. Further advantages include a relatively short synthesis time of about 1 to 5 h and the fact that a single precursor can be used to obtain several different products. Additionally, the calcination procedure is the only way to obtain pure phase Mn_5O_8 [28-33].

Here, we present the synthesis of nanocrystalline Mn(II) glycolate by a polyol process and demonstrate its suitability as a precursor in the synthesis of different manganese oxides. The polyol process is a well-known route for the synthesis of metal glycolates, usually yielding disc-shaped particles with diameters and thicknesses in the range of 1 to 3 μm and 100 to 250 nm, respectively [19,29,34,35]. By applying milder reaction conditions (i.e., decreasing the synthesis temperature and increasing the reaction time), we obtained homogeneous, rectangular Mn(II) glycolate nanocrystals with diameters less than 25 nm. The preparation of nanoscale precursor particles

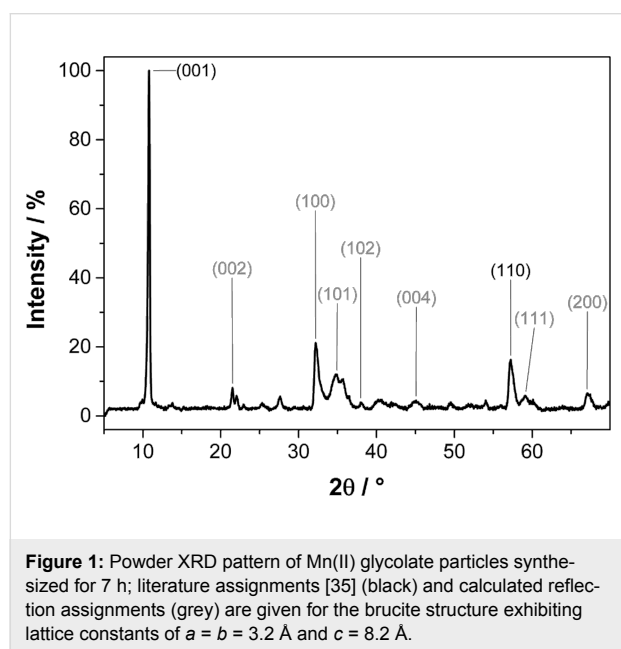
with uniform morphology is advantageous for the further synthesis of manganese oxides, because the control of the morphology and size of the particles is a major issue for their catalytic applications. The subsequent calcination process yielded Mn_3O_4 and Mn_5O_8 nanoparticles as well as mesoporous $\alpha\text{-Mn}_2\text{O}_3$ particles with high surface areas of 300, 30 and 20 m^2/g , respectively. The nanostructures of the obtained MnO_x particles make them attractive candidates as highly active compounds in the field of catalysis and other applications in the field of energy storage. Furthermore, the synthesis presented in this study provides easy access to three different nanostructured MnO_x species via one calcination process. This is advantageous for the investigation of the properties of the manganese oxides, as it rules out any synthesis-caused effects. The temperature- as well as the time-dependent phase transformation processes occurring during the oxidation of Mn(II) glycolate to Mn_3O_4 , Mn_5O_8 and $\alpha\text{-Mn}_2\text{O}_3$ were studied by in situ XRD measurements. A detailed study of the structural parameters of the manganese oxide products obtained after calcination in a temperature range from 320 to 550 $^\circ\text{C}$ in Ar and O_2 atmosphere was performed using powder XRD.

Results and Discussion

Precursor synthesis

The polyol process reported by Liu et al. [19] was modified to yield the Mn(II) glycolate precursor for the thermal decomposition to the various manganese oxides. During the heating of the compound to 170 $^\circ\text{C}$, a white precipitate appeared after 1 h, which was identified as manganese glycolate containing large impurities of the dehydrated educt Mn(II) acetate dihydrate and the product of a side reaction, manganese oxalate (MnC_2O_4 , see Supporting Information File 1 for the powder XRD pattern of the product mixture). In order to obtain the pure Mn(II) glycolate precursor having homogeneous particle morphology, the reaction was continued at 170 $^\circ\text{C}$ until a white precipitate of pure Mn(II) glycolate appeared. This was verified by the X-ray diffraction pattern of the product after 7 h of synthesis as depicted in Figure 1. This product can be assigned to the trigonal brucite-type structure ($P\bar{3}m1$) reported for Mn(II) glycolate by other groups [19,29,35]. A mean Scherrer crystallite size of 17 ± 8 nm was calculated for the Mn(II) glycolate particles. The interlayer distance along the [001] direction was calculated to be 8.2 \AA . This value corresponds to the lattice constant, c , and is consistent with reports by other groups who measured lattice constants of $c = 8.3$ \AA and $c = 8.27$ \AA for Mn and Co glycolate, respectively [34,35]. As Sun et al. [35] did not use tetraethylene glycolate (TEG) in their synthesis, it is proposed here that TEG anions are not part of the Mn(II) glycolate structure presented in this report, as c would be increased even beyond 8.2 \AA in this case. Hence, it can be concluded that TEG acts only as a stabilizing ligand to the Mn(II) glycolate parti-

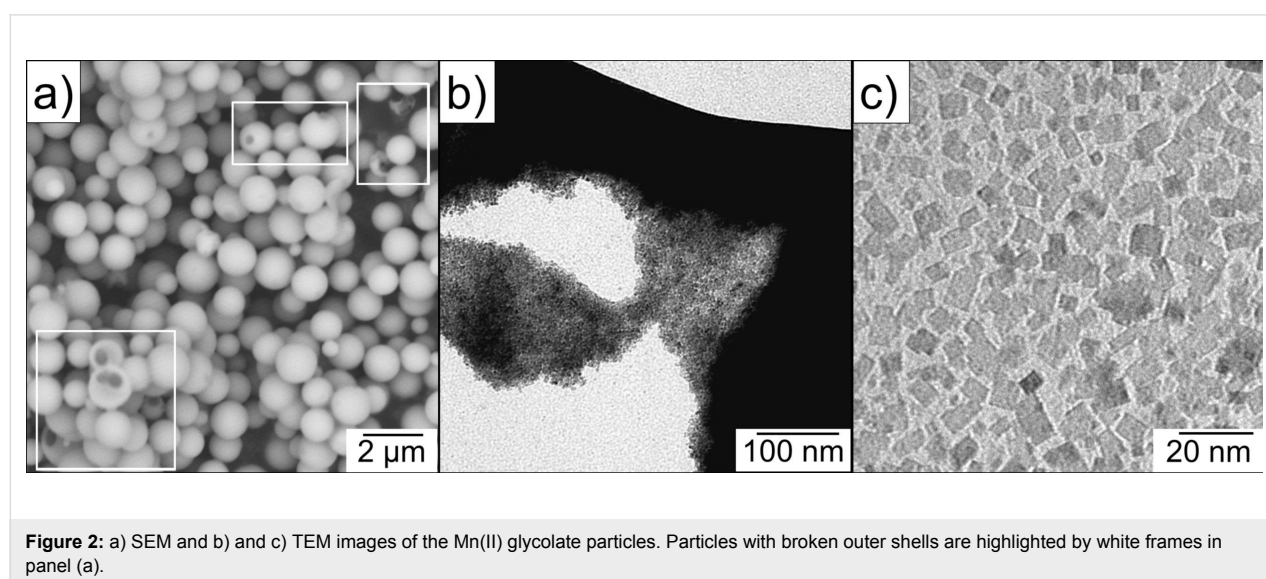
cles. This and the milder synthesis conditions applied are considered to be the reasons for the relatively small crystallite sizes, differing by one order of magnitude from the data presented to date in the literature [19,29,35]. Inorganic compounds with a brucite structure such as $\text{Mg}(\text{OH})_2$, $\text{Co}(\text{OH})_2$, $\text{Ca}(\text{OH})_2$ and $\text{Ni}(\text{OH})_2$, exhibit lattice constant c between 4.6 and 4.9 Å and a in the range from 3.1 to 3.6 Å. For Mn(II) glycolate, the Mn–Mn distance (corresponding to lattice constant a) was calculated to be 3.2 Å from the (110) reflection, which is also in accordance with the findings of Sun et al. [35] who proposed that the structure widening in the c direction is due to the long-chain alcoholate anions interconnecting the metal–oxygen sheets in the ab plane of the unit cell.



The morphology of the as-synthesized Mn(II) glycolate was investigated with SEM and TEM measurements. Figure 2a depicts SEM images of spherical Mn(II) glycolate particles with diameters up to 1 μm. These particles are hollow, which is deduced from the particles with broken outer shells (highlighted by white frames). Figure 2b shows a TEM image of one of these spherical particles, broken under the electron beam. A closer look reveals that the spheres are in fact agglomerates of rectangular Mn(II) glycolate nanoparticles with dimensions less than 15 nm (Figure 2c). The observed sizes of the particle are in good agreement with the calculated Scherrer crystallite sizes from the XRD pattern shown in Figure 1. The small dimensions of the particles make the synthesized Mn(II) glycolate a perfect precursor for the generation of manganese oxides by thermal decomposition processes.

The oxidation process to different MnO_x species

In order to investigate the temperature dependence of the oxidation process of Mn(II) glycolate, in situ X-ray diffractograms were recorded in the presence of O_2 while heating the precursor to 700 °C at a heating rate of 2 K/min (see Figure 3). The 2θ region of 17.6–23.8° was monitored during the measurement, as it contains the reflections of the species that are most likely to be generated during the oxidation process (21.5° (Mn(II) glycolate, □) [19], 18.0° (Mn_3O_4 , *) [36], 18.1° and 21.6° (Mn_5O_8 , +) [31], and 23.2° ($\alpha\text{-Mn}_2\text{O}_3$, ○) [37]). The reflection of Mn(II) glycolate at 21.5° is observed until a temperature of about 185 °C is reached, where a sudden decrease of the intensity (including the background intensity) is observed in the diffraction patterns due to the loss of organic species from the sample. This loss derives from the decomposition of the organic ligands and anions by oxidation; this is



dependent on the temperature as well as on the partial pressure of oxygen. The Mn_3O_4 reflection at 18.0° immediately evolves at about 185°C after the Mn(II) glycolate reflection has vanished. The appearance of the Mn_5O_8 reflection at 21.6° at about 350°C is accompanied by the decreasing intensity of the Mn_3O_4 reflection at 18.0° as well as an increasing intensity of the Mn_5O_8 reflection at 18.1° , which is attributed to the slow oxidation of Mn_3O_4 to Mn_5O_8 . The Mn_3O_4 reflection at 18.0° disappears at about 440°C , indicating a completed oxidation process of Mn_3O_4 to Mn_5O_8 . Both reflections assigned to Mn_5O_8 disappear at 550°C after the appearance of the intense $\alpha\text{-Mn}_2\text{O}_3$ reflection at 23.2° at a temperature of about 530°C .

Hence, in O_2 atmosphere, Mn_3O_4 is obtained at temperatures between 185 and 400°C , Mn_5O_8 between 400 and 550°C and $\alpha\text{-Mn}_2\text{O}_3$ above 530°C . This oxidation of Mn_3O_4 to Mn_5O_8 (rather than to Mn_2O_3) was found by Feitknecht [30] to take place during the heating of Mn_3O_4 particles at temperatures between 250 and 550°C in an atmosphere containing more than 5% O_2 . Feitknecht attributed this $\text{Mn}_3\text{O}_4/\text{Mn}_5\text{O}_8$ phase transformation to a one-phase mechanism for Mn_3O_4 particles exhibiting BET surface areas of more than $10\text{ m}^2/\text{g}$. That is, the small particle diameters provide sufficient reaction sites for oxidation

of the surface of the particles. Feitknecht also reported similar reflection intensities for Mn_3O_4 and Mn_5O_8 with a linear decrease and increase, respectively, during the oxidation process. The subsequent reduction process of Mn_5O_8 to $\alpha\text{-Mn}_2\text{O}_3$ was observed by several groups to take place even in oxygen-containing atmospheres at temperatures greater than 500°C [26,32,37].

The Mn(II) glycolate particles were calcined for 2 h in Ar and O_2 atmospheres at different temperatures between 320 and 550°C to investigate the dependence of the particle size, their morphology and the Mn^{x+} oxidation state in the resulting manganese oxide on the calcination temperature and atmosphere. The X-ray diffractograms of the resulting species as well as the reference patterns are shown in Figure 4; the crystalline phases observed in the XRD patterns are listed in Table 1.

The tetragonal Mn_3O_4 phase (ICDD 01-075-1560, $I4_1/amd$) is observed in the powder XRD patterns after calcination at temperatures between 320 and 450°C in both atmospheres. It is, however, obtained as a pure phase only at temperatures up to 400°C in Ar and up to 350°C in O_2 (see also Table 1). The presence of Mn_3O_4 in O_2 atmosphere could also be observed in

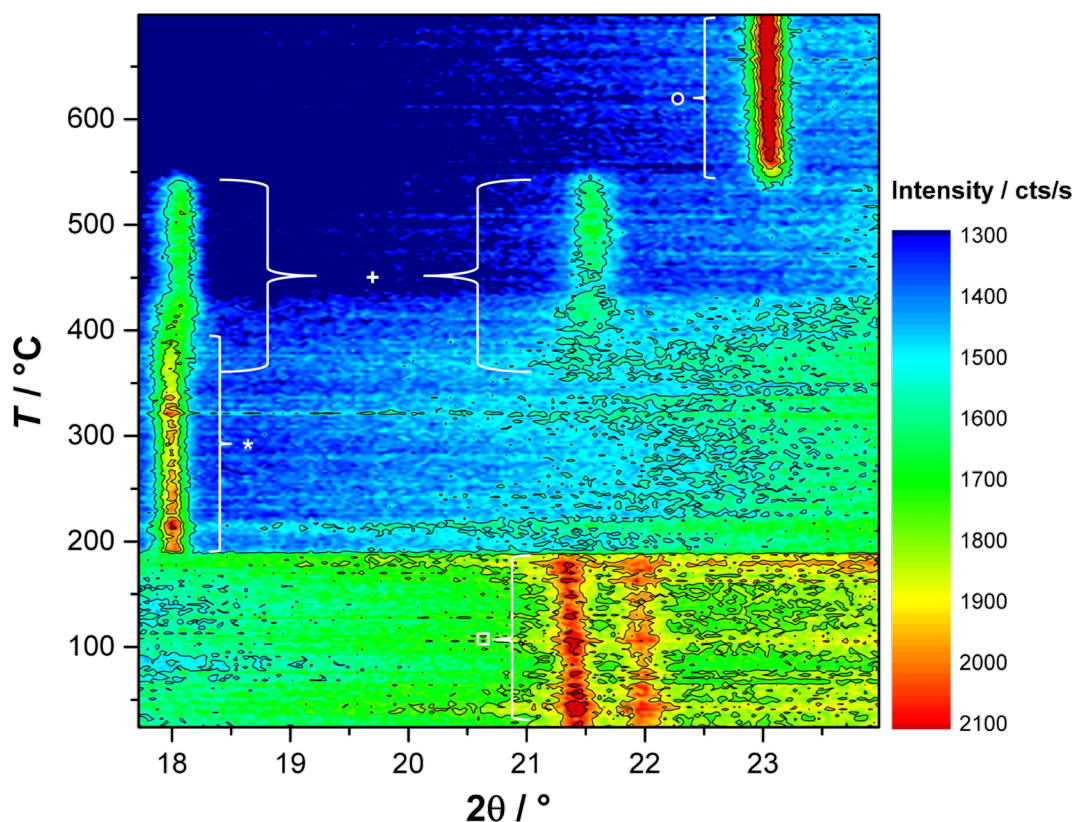
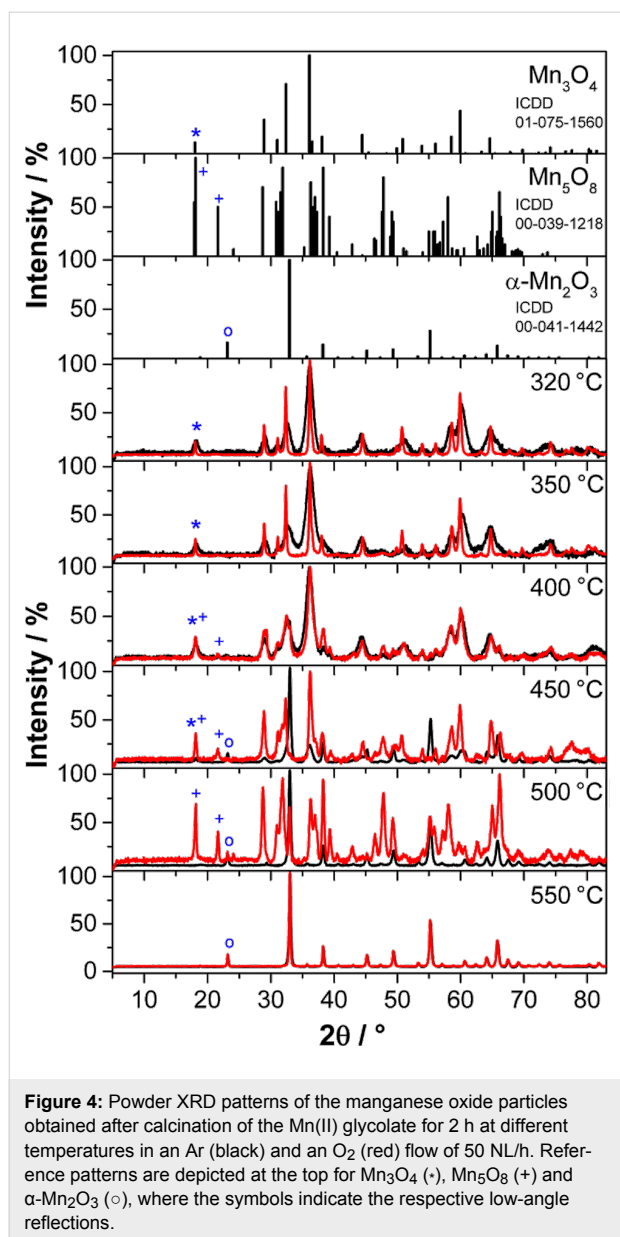


Figure 3: In situ XRD patterns recorded in a pure O_2 flow while heating the Mn(II) glycolate precursor to 700°C at 2 K/min ; reflexes denoted are: Mn(II) glycolate (\square), Mn_3O_4 (*), Mn_5O_8 (+) and $\alpha\text{-Mn}_2\text{O}_3$ (\circ).



the in situ XRD measurements up to a temperature of 440 °C (see Figure 3). The lattice parameters and crystallite sizes of the pure Mn₃O₄ samples obtained by calcination in Ar as well as O₂ atmospheres at 320 °C and 350 °C listed in Table 1 are obviously independent of the calcination temperature, but dependent on the calcination atmosphere. The samples obtained in Ar exhibit crystallite sizes of less than a third compared to those obtained in O₂. Furthermore, the lattice constants of Mn₃O₄ produced in Ar are smaller at all temperatures than those obtained by calcination in O₂ atmosphere. This could be due to oxygen vacancies, as the oxygen for the oxidation to Mn₃O₄ in pure Ar is only supplied by the manganese glycolate precursor and cannot be obtained from the gas atmosphere. The presence of oxygen vacancies is also supported by the less pronounced

variation of the lattice constants of Mn₃O₄ obtained at 320 °C and 350 °C in O₂ atmospheres, leading to the assumption of completely occupied oxygen sites in the structure of the oxide.

Cubic α-Mn₂O₃ (ICDD 00-041-1442, *Ia* $\bar{3}$) is obtained in Ar after calcination at temperatures between 450 and 550 °C and at 500–550 °C in O₂. Pure-phase α-Mn₂O₃, however, is only obtained after calcination at temperatures of 500 and 550 °C in Ar and at 550 °C in O₂ atmospheres (see also Table 1). The presence of α-Mn₂O₃ after calcination at 500 °C in O₂ does not support the observations made in the in situ XRD measurements (compare to Figure 3), where a generation of α-Mn₂O₃ from Mn₅O₈ in an O₂ atmosphere was only detected at temperatures above 530 °C. However, this is probably due to an additional time dependence of the phase transformation of Mn₅O₈ to α-Mn₂O₃, which was also suggested by Dimesso et al. [28]. In their report the α-Mn₂O₃ phase was observed to be the minor species second to Mn₅O₈ after calcination at 400 °C in air for 1 h, but was found to be the major species after calcination for 5 h at the same temperature. The lattice constants of the pure α-Mn₂O₃ phase obtained after calcination in Ar and O₂, are obviously independent of the temperature and the calcination atmosphere (see Table 1). Therefore, in contrast to the observations made for Mn₃O₄, the absence of O₂ in the calcination atmosphere does not lead to an increase in the concentration of oxygen vacancies in the α-Mn₂O₃ structure, which would be high enough to significantly change the lattice constants. The values of the Scherrer-derived crystallite sizes, however, suggest a temperature dependence of the obtained α-Mn₂O₃ particle size in Ar atmosphere, which was not the case for the Mn₃O₄ particles. The Scherrer-derived size of the crystallites of the pure phase α-Mn₂O₃ obtained in an O₂ atmosphere at 550 °C is one third larger than that calculated for particles obtained in Ar at the same temperature. Hence, similar to the Mn₃O₄ phases described above, the presence of O₂ in the calcination atmosphere yields larger crystallites of the same product.

No pure phase of monoclinic Mn₅O₈ (ICDD 00-039-1218, *C2/m*) could be obtained by calcination at temperatures between 320 and 550 °C for 2 h in both atmospheres. However, after calcination in O₂ atmosphere, a small fraction of Mn₅O₈ can be detected in the products obtained at 400 and 450 °C, while it forms the majority of the product obtained after calcination at 500 °C. This is in good agreement with the in situ XRD patterns recorded in O₂ atmosphere, where Mn₅O₈ was generated at about 350 °C and decomposed at 550 °C (see Figure 3).

In order to obtain pure-phase Mn₅O₈ particles, a longer calcination time of 5 h at 400 °C in an O₂ atmosphere was chosen based on the time profile from the in situ XRD measurements (see Supporting Information File 1 for further details).

Table 1: Crystalline manganese oxide phases obtained after calcination for 2 h in an Ar flow and an O₂ flow (50 NL/h) at different temperatures; mean Scherrer crystallite sizes (from all assigned reflections) and lattice parameters (from the (101) and (004) reflections of Mn₃O₄ as well as the (400) reflection of α-Mn₂O₃) were calculated for samples yielding pure phases.

Temperature [°C]	Atmosphere	Crystalline phase(s)	Lattice parameters [Å]	Crystallite size [nm]
320	Ar	Mn ₃ O ₄	<i>a</i> = 5.72 <i>c</i> = 9.38	11 ± 3
	O ₂	Mn ₃ O ₄	<i>a</i> = 5.75 <i>c</i> = 9.47	38 ± 11
350	Ar	Mn ₃ O ₄	<i>a</i> = 5.69 <i>c</i> = 9.44	10 ± 3
	O ₂	Mn ₃ O ₄	<i>a</i> = 5.74 <i>c</i> = 9.47	35 ± 10
400	Ar	Mn ₃ O ₄	<i>a</i> = 5.73 <i>c</i> = 9.39	9 ± 2
	O ₂	Mn ₃ O ₄ , Mn ₅ O ₈		
450	Ar	α-Mn ₂ O ₃ , Mn ₃ O ₄		
	O ₂	Mn ₃ O ₄ , Mn ₅ O ₈		
500	Ar	α-Mn ₂ O ₃	<i>a</i> = 9.41	27 ± 4
	O ₂	Mn ₅ O ₈ , α-Mn ₂ O ₃		
550	Ar	α-Mn ₂ O ₃	<i>a</i> = 9.40	34 ± 5
	O ₂	α-Mn ₂ O ₃	<i>a</i> = 9.41	44 ± 12

The properties of the Mn₅O₈ sample were investigated in more detail and compared to those of the Mn₃O₄ and α-Mn₂O₃ samples obtained by calcination for 2 h in Ar at 350 °C and at 550 °C, respectively. These Mn₃O₄ and α-Mn₂O₃ samples were chosen as they exhibit the most interesting properties for possible catalytic applications due to their small particle sizes.

The X-ray diffraction pattern of pure Mn₅O₈ obtained by calcination in an O₂ atmosphere at 400 °C for 5 h is shown in Figure 5. The Scherrer-derived crystallite size of this species is 22 ± 5 nm, and the lattice parameters of the monoclinic unit cell (ICDD 00-039-1218) are *a* = 10.40 Å, *b* = 5.73 Å and *c* = 4.87 Å with β = 109.6°, which is in good agreement with the data from literature (*a* = 10.34 Å, *b* = 5.72 Å and *c* = 4.85 Å with β = 109.25°) [31].

The temperature- and gas atmosphere-dependent oxidation process of Mn(II) glycolate to the manganese oxide species observed in the XRD patterns (see Figure 3 and Figure 4) was also investigated by thermogravimetric analysis (TGA). TGA measurements were recorded while heating the Mn(II) glycolate samples up to 700 °C with a heating rate of 2 K/min in an Ar (black) and an O₂/Ar (1:2) (red) flow, respectively.

In both atmospheres a mass loss of 2.1% due to loss of water from the samples is detected up to a temperature of 150 °C. In Ar atmosphere, a further mass loss of 5.7% occurs up to 320 °C, which we attribute to the decomposition of the organic ligands

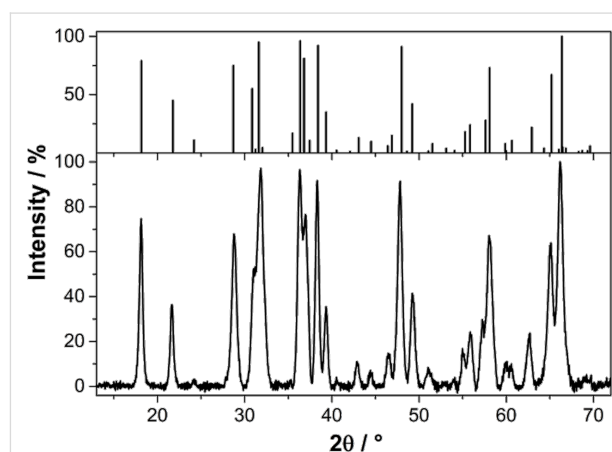


Figure 5: Powder XRD patterns of the Mn₅O₈ particles obtained by calcination of Mn(II) glycolate for 5 h at 400 °C in an O₂ flow of 50 NL/h; a reference pattern is given in the top panel (ICDD 00-039-1218).

(tetraethylene glycol and ethylene glycol), whose boiling points are in the temperature range of 150 °C to 320 °C. Subsequently, a mass loss of about 37% is detected up to 450 °C, which was also observed in TGA measurements of Ti(IV) glycolate by Jiang et al. [38] and was explained as a complete decomposition of the organic anions connecting the metal ions in that compound. Simultaneously, Mn(II) glycolate is oxidized to Mn₃O₄ and further to α-Mn₂O₃ between 185 °C to 450 °C, as was observed in the XRD measurements after calcination of the precursor for 2 h, as discussed above (see Figure 4). Although this oxidation process is accompanied by a decomposition of

the organic groups, XPS results showed the presence of approximately 25 atom % carbon in the α - Mn_2O_3 species obtained after calcination for 2 h at 550 °C in Ar atmosphere. This, however, will not have a significant effect on its application as an electrocatalyst, as the reference and substrate material for the catalysts consists of carbon.

The decomposition of the organic species of Mn(II) glycolate in combination with an immediate oxidation to Mn_3O_4 in O_2 atmosphere was observed at 185 °C in the in situ XRD measurement depicted in Figure 3. In the TGA measurement, however, a mass loss of 44% attributed to this process is detected between 150 and 250 °C. Hence, the observed mass loss includes the decomposition of organic species as well as the oxidation to Mn_3O_4 . The temperature delay of the processes can be explained by considering the smaller O_2 partial pressure of the atmosphere used for the TGA measurement. As both processes take place simultaneously, a clear assignment of the weight loss cannot be made. In order to investigate the processes subsequent to the large mass loss in the O_2 -containing atmosphere, a detailed view of the temperature region from 250 to 500 °C is shown in Figure 6b. Here, a mass increase of 0.54% is observed between 250 and 330 °C accompanied by a differential scanning calorimetry (DSC) signal of an exothermal phase transformation at 270 °C indicating a partial oxidation of Mn_3O_4 to Mn_5O_8 . This is in good agreement with the development of the Mn_5O_8 phase observed at about 350 °C in the in situ XRD measurements (see Figure 3). The expected mass gain by complete oxidation to Mn_5O_8 of 5.59% is, however, much larger. Gillot et al. [27] proposed that heating rates between 1.2 and 2.5 K/min could lead to a direct oxidation of Mn_3O_4 to α - Mn_2O_3 even in O_2 atmosphere, which would result in an expected mass gain of 0.97%. As both the direct oxidation of Mn_3O_4 to α - Mn_2O_3 and the oxidation via Mn_5O_8 would result in larger mass increases than the one observed in the measurement (0.54%), it is suggested that the decomposition of the organic species is not complete at a temperature of 330 °C. However, the subsequent mass loss of 1.60% from 330 to 480 °C, a DSC signal of an exothermal phase transformation at 480 °C, and the XRD measurements presented in this report (see Figure 3 and Figure 4) indicate the presence of Mn_5O_8 . This mass loss again is lower than the expected value of 2.03% for a complete conversion of Mn_5O_8 to α - Mn_2O_3 , which indicates that less α - Mn_2O_3 is formed from Mn_5O_8 than expected. Hence, in an O_2/Ar atmosphere, α - Mn_2O_3 is generated partially from Mn_5O_8 and partially by direct oxidation from Mn_3O_4 .

The increase and decrease in mass in the presence of gaseous O_2 was proposed to be due to slow seed crystal oxidation of Mn_3O_4 to Mn_5O_8 for particles with BET surfaces larger than

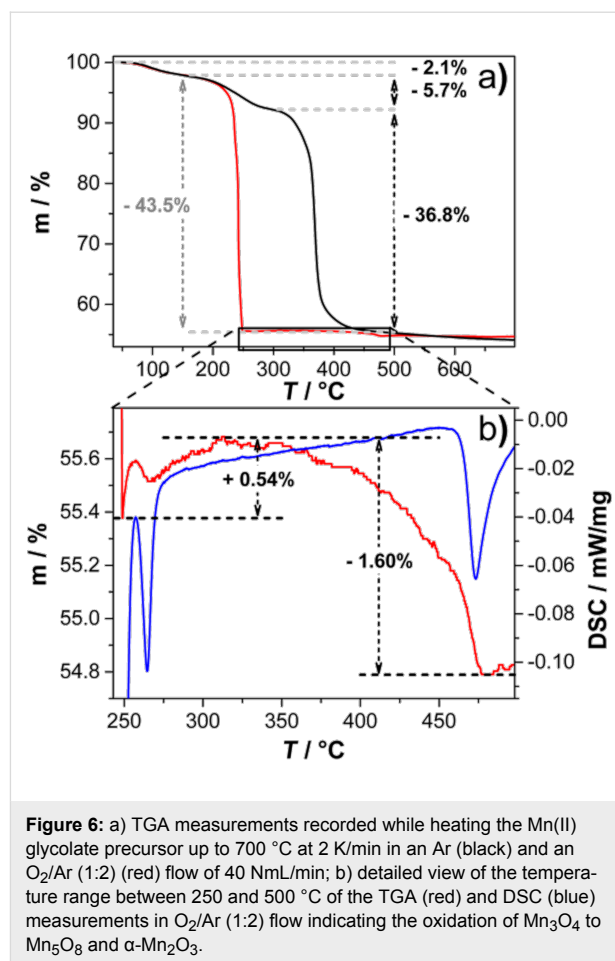


Figure 6: a) TGA measurements recorded while heating the Mn(II) glycolate precursor up to 700 °C at 2 K/min in an Ar (black) and an O_2/Ar (1:2) (red) flow of 40 NmL/min; b) detailed view of the temperature range between 250 and 500 °C of the TGA (red) and DSC (blue) measurements in O_2/Ar (1:2) flow indicating the oxidation of Mn_3O_4 to Mn_5O_8 and α - Mn_2O_3 .

10 m^2/g and their subsequent transformation to α - Mn_2O_3 [29,30].

In order to characterize the size of the particles and the active surface areas, pure Mn_3O_4 , Mn_5O_8 and α - Mn_2O_3 species obtained by calcination of the Mn(II) glycolate precursor at temperatures of 350, 400 and 550 °C were characterized by TEM and BET measurements. The TEM images of the Mn_3O_4 and Mn_5O_8 samples are shown in Figure 7a,b; the sizes of the particles observed in TEM are in good agreement with the Scherrer-derived crystallite sizes calculated from the XRD patterns (see Figure 4 for comparison). The Mn_3O_4 sample shown in Figure 7a consists of a network of nanoparticles with diameters less than 10 nm and voids between the particles of about the same size. The same is true for the Mn_5O_8 sample in Figure 7b, but here the nanoparticles with diameters of up to 30 nm are obviously packed more densely. We attribute this to the increased temperature and duration of the calcination process, as well as to the presence of O_2 in the atmosphere, which leads to larger particles, as previously discussed (see discussion for Figure 4). The α - Mn_2O_3 sample obtained by calcination in an Ar atmosphere (see Figure 7c,d), however,

contains splinter-like pieces in the μm range (approximately 1–2 μm in the given TEM image) with a high concentration of holes with diameters of up to 20 nm, rather than individual nanoparticles. This manner of porosity for $\alpha\text{-Mn}_2\text{O}_3$ was also confirmed by N_2 adsorption–desorption measurements (see Figure 8). Mesoporosity in hexagonally shaped $\alpha\text{-Mn}_2\text{O}_3$ particles and circular Mn_2O_3 discs obtained by calcination at temperatures above 600 °C was reported by several groups [17,37]. Ren et al. suggested that the mesopores are derived from a sequence of processes including Mn_5O_8 nanoparticle growth, rearrangement and merging during the transformation to $\alpha\text{-Mn}_2\text{O}_3$ [37]. As the phase of Mn_5O_8 was not observed after calcination in Ar atmosphere, we propose that the presence of pores in the $\alpha\text{-Mn}_2\text{O}_3$ particles reported here results from the analog growth, rearrangement and merging processes of the Mn_3O_4 nanoparticles.

The considerably smaller size of the crystallites obtained from the broadening of the XRD reflections of $\alpha\text{-Mn}_2\text{O}_3$ is another argument for the porosity of these particles, as the pore walls in this case represent boundaries of the crystalline domains. Because these domains are regarded as Scherrer crystallites, we conclude that the obtained sizes are the mean distances between the pores as well as the minimum diameter of the $\alpha\text{-Mn}_2\text{O}_3$ particles.

From the isotherms recorded during N_2 adsorption–desorption measurements (see Figure 8a) specific BET surface areas of 302, 30 and 20 m^2/g were calculated for the Mn_3O_4 , Mn_5O_8 and $\alpha\text{-Mn}_2\text{O}_3$ samples, respectively. The porosity of the $\alpha\text{-Mn}_2\text{O}_3$ particles observed in the TEM images (see Figure 7c,d) is also supported by the N_2 adsorption–desorption isotherms, which exhibit hysteresis. As hysteresis is also

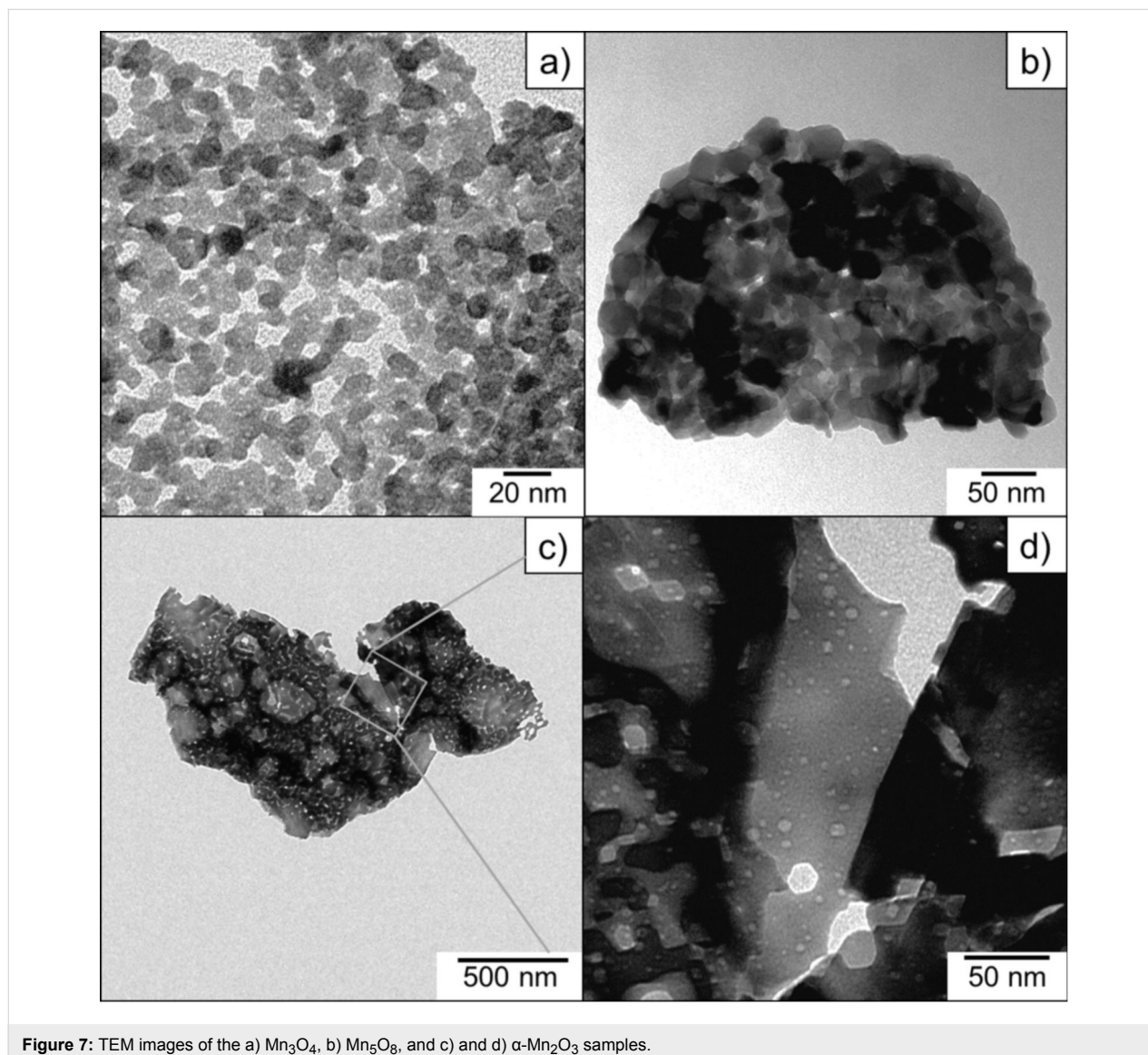


Figure 7: TEM images of the a) Mn_3O_4 , b) Mn_5O_8 , and c) and d) $\alpha\text{-Mn}_2\text{O}_3$ samples.

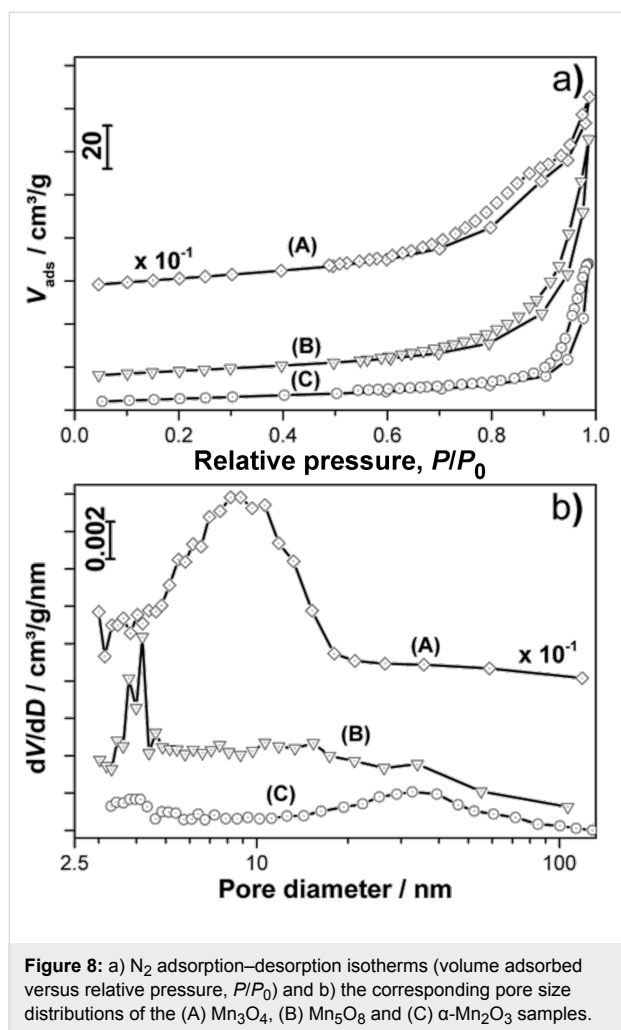


Figure 8: a) N_2 adsorption–desorption isotherms (volume adsorbed versus relative pressure, P/P_0) and b) the corresponding pore size distributions of the (A) Mn_3O_4 , (B) Mn_5O_8 and (C) $\alpha\text{-Mn}_2\text{O}_3$ samples.

observed in the Mn_3O_4 and Mn_5O_8 nanoparticle isotherms (but not supported by observations made in the TEM images for these species, see Figure 7a,b), two different definitions of porosity can be applied for the different manganese oxide species. The pore size distributions depicted in Figure 8b show a pore diameter distribution between 3 and 20 nm with a mean pore diameter of 8.2 nm for the Mn_3O_4 sample. The porosity of the Mn_3O_4 nanoparticles can be explained by considering the voids between the particles in the network as the “pores” detected in the N_2 adsorption–desorption measurements. This assumption is in good agreement with the similar sizes of the voids and nanoparticles observed in the TEM image (compared with Figure 7a). The same “pore definition” can be applied to the Mn_5O_8 sample exhibiting pore sizes between 3 and 5 nm with a comparably small mean pore size of 4.2 nm, probably due to the dense network of the particles observed in the TEM image (compared to Figure 7b). The $\alpha\text{-Mn}_2\text{O}_3$ sample does not contain nanoparticles, but exhibits a pore size distribution between 3 and 5 nm as well as 10 and 90 nm with a mean diameter of 32.6 nm. In accordance with the TEM images (see

Figure 7c,d for comparison) and the lowest BET surface area of all the samples, these pores do not derive from voids in the nanoparticle network but rather from the mesoporosity of the splinter-like pieces. A surface area of approximately $20 \text{ m}^2/\text{g}$ and pore diameters from 4 to 7 nm were also reported for Mn_2O_3 discs synthesized for the use as electrode material by Zhang et al. [17]. However, we believe a larger pore size to be advantageous for application as electrocatalysts, as electrochemical processes often produce solid products, which might easily clog pores in the micro- and meso-porous range.

The specific surface areas of Mn_3O_4 and Mn_5O_8 are in good agreement with the sizes of the particles observed in the TEM images and calculated from the XRD patterns, as smaller particles generally exhibit larger surface areas. However, the $\alpha\text{-Mn}_2\text{O}_3$ particles, which are one order of magnitude larger, exhibit a high specific BET surface area comparable to that of the Mn_5O_8 nanoparticles. Two explanations for this large specific surface are proposed: the lower molar weight of $\alpha\text{-Mn}_2\text{O}_3$ compared to Mn_5O_8 (resulting in a larger specific surface area), and the mesoporosity of the $\alpha\text{-Mn}_2\text{O}_3$, which was already observed in the TEM images (see Figure 7c,d).

Electrocatalytic activities of the MnO_x species

In order to investigate the electrocatalytic activity of the synthesized MnO_x species for the oxygen reduction reaction (ORR), linear sweep measurements were carried out.

Figure 9 shows linear sweep measurements recorded at 50 mV/s comparing the activity of various 10% $\text{MnO}_x/\text{carbon}$ electrodes to a pure carbon electrode as a reference material for the ORR in aprotic electrolyte. The ORR peak potentials as well as the apparent reaction rate constant, k_{app}^0 , for the different electrode materials are summarized in Table 2. The reaction rate constant was calculated from:

$$j_0 = n \cdot F \cdot C_{\text{O}_2} \cdot k_{\text{app}}^0, \quad (1)$$

where j_0 is the cathodic exchange current density (obtained from the Tafel plots of the linear sweep measurements), $n = 1$ is the number of transferred electrons, F is the Faraday constant, and $C_{\text{O}_2} = 2.1 \cdot 10^{-6} \text{ mol cm}^{-3}$ is the oxygen solubility in DMSO [39].

The mean ORR peak potential of the carbon reference material given in Table 2 is observed at 2.58 V. The only MnO_x species with a significant increase of the ORR potential of 100 mV with respect to the carbon as well as the other MnO_x/C electrodes is the mesoporous $\alpha\text{-Mn}_2\text{O}_3$ catalyst. The obvious activity is

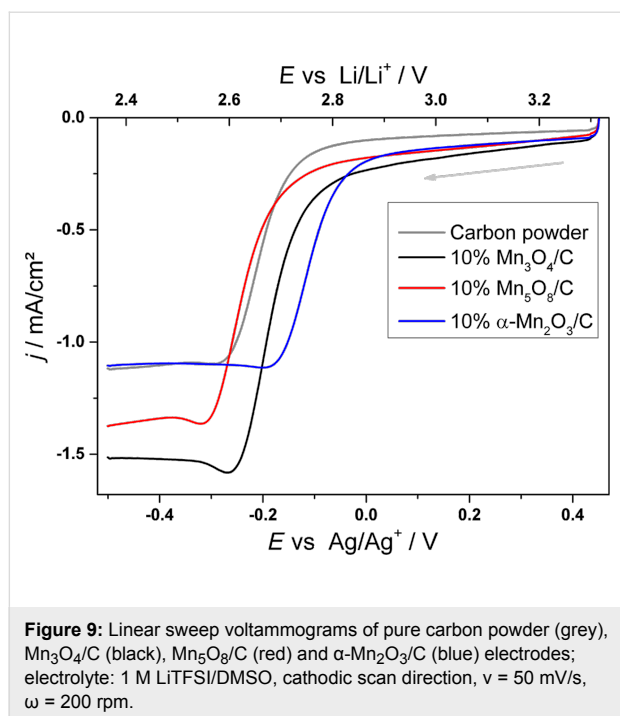


Table 2: ORR potentials and reaction rate constants obtained from the linear sweep measurements recorded at $v = 50$ mV/s.

	$E_{\text{peak vs Li/Li}^+}$ [V]	k_{app}^0 [10^{-4} cm/s]
Carbon (C)	2.58 ± 0.02	1.2 ± 1.1
Mn ₃ O ₄ /C	2.58 ± 0.08	2.6 ± 1.3
Mn ₅ O ₈ /C	2.58 ± 0.07	2.7 ± 2.3
α-Mn ₂ O ₃ /C	2.68 ± 0.05	4.5 ± 2.5

reflected in the approximately four- and two-fold larger apparent ORR rate constant k_{app}^0 compared to the carbon and the other MnO_x/C electrodes, respectively.

A detailed kinetic and mechanistic study on the electrocatalytic activities of the different MnO_x species for the aprotic oxygen reduction reaction is reported elsewhere [40].

Conclusion

In summary, a polyol synthesis was presented yielding rectangular, Mn(II) glycolate nanoparticles with dimensions of 17 ± 8 nm. Particle sizes of less than 100 nm are reported here for the first time. We attribute this small size of the particles to the stabilizing tetraethylene glycol ligand used during the synthesis, as well as milder reaction conditions compared with other reports (i.e., a decreased temperature and a longer reaction time). In situ XRD measurements showed the sequence of time- and temperature-dependent phase transformations during

oxidation of the Mn(II) glycolate precursor to α-Mn₂O₃ via Mn₃O₄ and Mn₅O₈ in O₂ atmosphere. Structural and morphological investigations revealed the dependence of the lattice constants and particle sizes of the MnO_x species on the calcination temperatures in a range from 320 to 550 °C as well as on Ar and O₂ atmospheres. Based on the results of these measurements, several manganese oxide species were synthesized by calcination of Mn(II) glycolate particles in argon and oxygen atmosphere at different temperatures. The calcination process yielded Mn₃O₄ nanoparticles with dimensions of about 10 nm and a surface area of 302 m²/g, Mn₅O₈ nanoparticles with diameters of 22 nm and a surface area of 30 m²/g as well as mesoporous α-Mn₂O₃ particles with mean pore diameters of about 33 nm and a surface area of 20 m²/g. The small dimensions of the particles and large surface areas of the manganese oxides presented here result from use of nanostructured precursor particles. Linear sweep measurements showed the activity of the mesoporous α-Mn₂O₃ species for the oxygen reduction reaction in aprotic media with respect to the observed potentials as well as an enhanced kinetic activity. The catalytic activity of different manganese oxides can be enhanced by a larger surface area, resulting from small particle dimensions or mesoporosity. This makes our synthesis a suitable process to obtain manganese oxides having properties of particular interest for electrochemical and chemical catalysis. Furthermore, the synthesis of manganese oxides via one route reported here is of additional interest, as it excludes any synthesis-caused effects on the products and allows investigation on the catalytic effect of similarly synthesized manganese oxides with different properties.

Experimental Materials

Manganese(II) acetate tetrahydrate (MnAc₂, >99%, pure) and ethylene glycol (EG, >99.5%, p.a.) were purchased from Carl-Roth. Tetraethylene glycol (TEG, 99%) was delivered by Sigma-Aldrich. For the electrode preparation, a 10 wt % Nafion[®]/water solution was purchased from Sigma-Aldrich, analytical reagent-grade ethanol from Fisher Scientific, and Vulcan[®] XC72R carbon powder was obtained from Cabot. For electrochemical measurements, reagent-grade lithium bis(trifluoromethylsulfonyl)imide (LiTFSI) was purchased from Merck KGaA and dimethyl sulfoxide (DMSO, anhydrous, ≥99.9%) from Sigma-Aldrich. All chemicals were used without further purification.

Synthesis of Mn(II) glycolate

In a typical reaction, 1 mmol (0.246 g) MnAc₂ was mixed with 3 mmol (3 mL) TEG and added to 30 mL EG in a three-neck round-bottom flask. The solution was heated to 170 °C while stirring. Upon heating, the solution turned brown at a tempera-

ture of about 110 °C, and after further heating for about 1 h at 170 °C, a white precipitate appeared that disappeared again after 1 h. The solution was stirred for another 4 h at 170 °C until a white precipitate appeared again which indicated the formation of the Mn(II) glycolate particles. The product was stirred for another hour at 170 °C to complete the reaction and was subsequently cooled down to room temperature. The white powder was centrifuged and washed at least five times with ethanol to remove any impurities. Subsequently, the white product was dried under Ar flow.

Synthesis of Mn₃O₄, Mn₅O₈ and α -Mn₂O₃

The obtained Mn(II) glycolate powder was calcined in an Ar flow of 50 NL/h for 2 h at 350 °C and at 550 °C yielding Mn₃O₄ and α -Mn₂O₃, respectively. Mn₅O₈ was obtained by calcination of the precursor in an O₂ flow of 50 NL/h for 5 h at 400 °C.

Characterization methods

Transmission electron microscopy (TEM) was carried out with a Zeiss EM 902A microscope with an acceleration voltage of 80 kV. For high resolution TEM (HR-TEM) measurements a JEOL JEM2100F microscope with an acceleration voltage of 200 kV was used. The samples for TEM and HR-TEM measurements were prepared by depositing a drop of an ethanol emulsion of the powder on a carbon-coated copper grid and drying at room temperature.

Scanning electron microscopy (SEM) was carried out with an Oxford INCA system employing a PentaFET Precision INCA X-act detector integrated into the Hitachi S-3200N microscope. The sample was prepared by depositing an ethanol emulsion of the sample onto an Al substrate and drying at room temperature.

For X-ray diffraction (XRD), a PANalytical X'Pert Pro MPD diffractometer was used operating with Cu K α radiation, Bragg-Brentano θ -2 θ geometry and a goniometer radius of 240 mm. Samples for XRD measurements were prepared by placing the powder onto low-background silicon sample holders. Different atmospheres were used as mentioned in the text. The crystallite sizes of the samples were calculated from all assigned reflections via the Scherrer equation. The lattice parameters were obtained with the Bragg equation from assigned diffraction reflections.

In situ XRD measurements were performed in the same geometry using a high temperature chamber from Anton Paar (HTK 1200N). The temperature profile measurement was recorded while heating the powder sample from 25 to 700 °C with a heating rate of 2 K/min. The time profile measurement (shown in Supporting Information File 1) was conducted by heating the

powder sample from 25 to 400 °C with a heating rate of 18 K/min and subsequent constant heating at 400 °C for 350 min. The powder sample was placed on a corundum sample holder. During the measurement the thermal expansion was corrected automatically. The measurements were performed in an O₂ flow.

Thermogravimetric analysis (TGA) and differential scanning calorimetry (DSC) were carried out with a Netzsch STA 449 F3 Jupiter thermo-analysis system. The sample was deposited in an Al₂O₃ crucible and heated from 35 to 700 °C with a heating rate of 2 K/min in an O₂(6.0)/Ar(5.0) (1:2) and an Ar(5.0) gas flow of 40 NmL/min.

The porosity of the manganese oxides was determined by N₂ adsorption–desorption measurements. Prior to the measurement, the material was kept for 18 h at 180 °C under vacuum to remove any residual gas and moisture from the sample. The adsorption–desorption isotherms were measured employing a Quantachrome Nova 2000E device at 77 K. The Brunauer–Emmet–Teller (BET) method was used to determine the complete inner surfaces S_0 and the Barrett–Joyner–Halenda (BJH) method for mesopore surface analysis as well as the determination of pore size distributions.

Electrode preparation

The catalyst/carbon ink for the powder electrodes was prepared by mixing and grinding 90 mg Vulcan[®] XC72R carbon powder with 10 mg of MnO_x catalyst. This active material was dispersed in ethanol and ultrasonicated for 20 min. As a binder material, 0.1 wt % Nafion/water solution was added to the catalyst/carbon paste and ultrasonicated for another 20 min. A 10 μ L drop of the ink was applied on a glassy carbon disc ($d = 0.5$ cm) and dried for 12 h at 80 °C. The 10 wt % catalyst loading of the prepared electrodes equals 4.8 μ g per electrode or 24.4 μ g cm⁻².

Electrochemical measurements

For linear sweep voltammetry measurements, a Gamry Instruments Reference 600 Potentiostat was used. The measurements were carried out on a rotating disc electrode (RDE) in a glove box in Ar atmosphere at ambient temperature. For the electrochemical setup, glassy carbon (Pine Research Instrumentation, electrode model no. AFE3T050GC) and carbon/catalyst-coated glassy carbon discs (see above) served as working electrodes. A polished Ag wire and a Pt disc were used as reference and counter electrodes, respectively. 1 M LiTFSI/DMSO was used as the electrolyte, which was saturated with pure O₂ for 25 min before the start of the measurement. The linear sweep measurements were recorded at a scan rate of $v = 50$ mV/s and a rotational frequency of $\omega = 200$ rpm.

Supporting Information

The supporting information features the powder XRD pattern of Mn(II) glycolate particles after 1 h of synthesis at 170 °C in addition to in situ XRD patterns of the time-dependent oxidation of Mn₃O₄ to Mn₅O₈ at 400 °C in O₂.

Supporting Information File 1

Additional XRD experimental data.

[<http://www.beilstein-journals.org/bjnano/content/supplementary/2190-4286-6-6-S1.pdf>]

Acknowledgements

We thank Magdalena Bogacka for conducting the TGA/DSC measurements. We gratefully acknowledge the funding of the EWE Research Group “Thin Film Photovoltaics” by the EWE AG, Oldenburg, Germany, as well as funding by the government of Lower Saxony (Germany).

References

- Owens, B. B.; Passerini, S.; Smyrl, W. H. *Electrochim. Acta* **1999**, *45*, 215–224. doi:10.1016/S0013-4686(99)00205-4
- Park, K.-W. *J. Mater. Chem. A* **2014**, *2*, 4292–4298. doi:10.1039/c3ta14223j
- Xu, M.-W.; Niu, Y.-B.; Bao, S.-J.; Li, C. M. *J. Mater. Chem. A* **2014**, *2*, 3749–3755. doi:10.1039/c3ta14211f
- Gil, A.; Gandía, L. M.; Korili, S. A. *Appl. Catal., A* **2004**, *274*, 229–235. doi:10.1016/j.apcata.2004.07.004
- Mellan, T. A.; Maenettja, K. P.; Ngoepe, P. E.; Woodley, S. M.; Catlow, C. R. A.; Grau-Crespo, R. *J. Mater. Chem. A* **2013**, *1*, 14879–14887. doi:10.1039/c3ta13559d
- Feng, Q.; Kanoh, H.; Ooi, K. J. *Mater. Chem.* **1999**, *9*, 319–333. doi:10.1039/a805369c
- Kaptelj, F.; Singoredjo, L.; Andreini, A.; Moulijn, J. A. *Appl. Catal., B: Environ.* **1994**, *3*, 173–189. doi:10.1016/0926-3373(93)E0034-9
- Xiao, J.; Wan, L.; Wang, X.; Kuang, Q.; Dong, S.; Xiao, F.; Wang, S. *J. Mater. Chem. A* **2014**, *2*, 3794–3800. doi:10.1039/c3ta14453d
- Su, H.-Y.; Gorlin, Y.; Man, I. C.; Calle-Vallejo, F.; Nørskov, J. K.; Jaramillo, T. F.; Rossmeisl, J. *Phys. Chem. Chem. Phys.* **2012**, *14*, 14010–14022. doi:10.1039/c2cp40841d
- Ramírez, A.; Friedrich, D.; Kunst, M.; Fiechter, S. *Chem. Phys. Lett.* **2013**, *568–569*, 157–160. doi:10.1016/j.cplett.2013.03.054
- Najafpour, M. M.; Rahimi, F.; Amini, M.; Nayeri, S.; Bagherzadeh, M. *Dalton Trans.* **2012**, *41*, 11026–11031. doi:10.1039/c2dt30553d
- Ogasawara, T.; Débart, A.; Holzapfel, M.; Novák, P.; Bruce, P. G. *J. Am. Chem. Soc.* **2006**, *128*, 1390–1393. doi:10.1021/ja056811q
- Débart, A.; Bao, J.; Armstrong, G.; Bruce, P. G. *J. Power Sources* **2007**, *174*, 1177–1182. doi:10.1016/j.jpowsour.2007.06.180
- Giordani, V.; Freunberger, S. A.; Bruce, P. G.; Tarascon, J.-M.; Larcher, D. *Electrochem. Solid-State Lett.* **2010**, *13*, A180–A183. doi:10.1149/1.3494045
- Cheng, H.; Scott, K. *Appl. Catal., B: Environ.* **2011**, *108–109*, 140–151. doi:10.1016/j.apcatb.2011.08.021
- Jung, K.-N.; Riaz, A.; Lee, S.-B.; Lim, T.-H.; Park, S.-J.; Song, R.-H.; Yoon, S.; Shin, K.-H.; Lee, J.-W. *J. Power Sources* **2013**, *244*, 328–335. doi:10.1016/j.jpowsour.2013.01.028
- Zhang, Y.; Yan, Y.; Wang, X.; Li, G.; Deng, D.; Jiang, L.; Shu, C.; Wang, C. *Chem. – Eur. J.* **2014**, *22*, 6126–6130. doi:10.1002/chem.201304935
- Lei, S.; Tang, K.; Fang, Z.; Liu, Q.; Zheng, H. *Mater. Lett.* **2006**, *60*, 53–56. doi:10.1016/j.matlet.2005.07.070
- Liu, L.; Yang, Z.; Liang, H.; Yang, H.; Yang, Y. *Mater. Lett.* **2010**, *64*, 891–893. doi:10.1016/j.matlet.2010.01.054
- Azzoni, C. B.; Mozzati, M. C.; Galinetto, P.; Paleari, A.; Massarotti, V.; Capsoni, D.; Bini, M. *Solid State Commun.* **1999**, *112*, 375–378. doi:10.1016/S0038-1098(99)00368-3
- Cushing, B. L.; Kolesnichenko, V. L.; O'Connor, C. J. *Chem. Rev.* **2004**, *104*, 3893–3946. doi:10.1021/cr030027b
- Gui, Z.; Fan, R.; Mo, W.; Chen, X.; Yang, L.; Hu, Y. *Mater. Res. Bull.* **2003**, *38*, 169–176. doi:10.1016/S0025-5408(02)00983-2
- Javed, Q.; Feng-Ping, W.; Rafique, M. Y.; Toufiq, A. M.; Iqbal, M. Z. *Chin. Phys. B* **2012**, *21*, 117311–117317. doi:10.1088/1674-1056/21/11/117311
- Yuan, Z.-Y.; Ren, T.-Z.; Du, G.; Su, B.-L. *Chem. Phys. Lett.* **2004**, *389*, 83–86. doi:10.1016/j.cplett.2004.03.064
- Liu, L.; Yang, H.; Wei, J.; Yang, Y. *Mater. Lett.* **2011**, *65*, 694–697. doi:10.1016/j.matlet.2010.11.042
- Dhaouadi, H.; Ghodbane, O.; Hosni, F.; Touati, F. *ISRN Spectrosc.* **2012**, *2012*, 1–8. doi:10.5402/2012/706398
- Gillot, B.; El Guendouzi, M.; Laarj, M. *Mater. Chem. Phys.* **2001**, *70*, 54–60. doi:10.1016/S0254-0584(00)00473-9
- Dimesso, L.; Heider, L.; Hahn, H. *Solid State Ionics* **1999**, *123*, 39–46. doi:10.1016/S0167-2738(99)00107-1
- Larcher, D.; Sudant, G.; Patrice, R.; Tarascon, J. *Chem. Mater.* **2003**, *15*, 3543–3551. doi:10.1021/cm030048m
- Feitknecht, W. *Pure Appl. Chem.* **1964**, *9*, 423–440. doi:10.1351/pac196409030423
- Oswald, H. R.; Wampetich, M. J. *Helv. Chim. Acta* **1967**, *50*, 2023–2034. doi:10.1002/hlca.19670500736
- Punnoose, A.; Magnone, H.; Seehra, M. S. *IEEE Trans. Magn.* **2001**, *37*, 2150–2152. doi:10.1109/20.951107
- Thota, S.; Prasad, B.; Kumar, J. *Mater. Sci. Eng., B* **2010**, *167*, 153–160. doi:10.1016/j.mseb.2010.01.049
- Chakroune, N.; Viau, G.; Ammar, S.; Jouini, N.; Gredin, P.; Vaulay, M. J.; Fiévet, F. *New J. Chem.* **2005**, *29*, 355–361. doi:10.1039/b411117f
- Sun, Y.; Hu, X.; Luo, W.; Huang, Y. *J. Mater. Chem.* **2012**, *22*, 19190–19195. doi:10.1039/c2jm32036c
- Aminoff, G. Z. *Kristallogr., Kristallgeom., Kristallphys., Kristallchem.* **1926**, *64*, 475–490.
- Ren, T.-Z.; Yuan, Z.-Y.; Hu, W.; Zou, X. *Microporous Mesoporous Mater.* **2008**, *112*, 467–473. doi:10.1016/j.micromeso.2007.10.025
- Jiang, X.; Wang, Y.; Herricks, T.; Xia, Y. *J. Mater. Chem.* **2004**, *14*, 695–703. doi:10.1039/b313938g
- Sawyer, D. T.; Chiericato, G., Jr.; Angells, C. T.; Nanni, E. J., Jr.; Tsuchiya, T. *Anal. Chem.* **1982**, *54*, 1720–1724. doi:10.1021/ac00248a014
- Augustin, M.; Yezerka, O.; Fenske, D.; Bardenhagen, I.; Westphal, A.; Knipper, M.; Plaggenborg, T.; Kolny-Olesiak, J.; Parisi, J. *Electrochim. Acta* **2014**, submitted.

License and Terms

This is an Open Access article under the terms of the Creative Commons Attribution License (<http://creativecommons.org/licenses/by/2.0>), which permits unrestricted use, distribution, and reproduction in any medium, provided the original work is properly cited.

The license is subject to the *Beilstein Journal of Nanotechnology* terms and conditions: (<http://www.beilstein-journals.org/bjnano>)

The definitive version of this article is the electronic one which can be found at:
[doi:10.3762/bjnano.6.6](https://doi.org/10.3762/bjnano.6.6)